Scientific Reports

https://doi.org/10.1038/s41598-025-33033-3

Article in Press

A simulation-based plasmonic terahertz nanosensor with graphene-enhanced sensitivity for diabetes monitoring

Received: 20 October 2025

Accepted: 15 December 2025

Published online: 20 December 2025

Cite this article as: Rafighirani Y. & Javidan J. A simulation-based plasmonic terahertz nanosensor with graphene-enhanced sensitivity for diabetes monitoring. *Sci Rep* (2025). https://doi.org/10.1038/s41598-025-33033-3

Yousef Rafighirani & Javad Javidan

A Simulation-Based Plasmonic Terahertz Nanosensor with Graphene-Enhanced Sensitivity for Diabetes Monitoring

Yousef Rafighirani[1], Javad Javidan [1,*]

[1]Department of Electrical and Computer Engineering, University of Mohaghegh Ardabili, Ardabil, Iran.

[*]Corresponding author: javidan@uma.ac.ir

Abstract:

We report a dual-mode terahertz plasmonic nanosensor based on a novel graphene–SiO_2–gold multilayer architecture, engineered for rapid and highly sensitive non-invasive detection of blood glucose concentration via refractive index sensing. This is the first sensor that simultaneously achieves two sharp, independently tunable resonant modes at 2.48–2.50 THz (mode one) and 6.01–6.12 THz (mode two) through the synergistic interaction of localized surface plasmon resonance (LSPR) and near-perfect impedance matching. The second mode exhibits an outstanding sensitivity of 4.5 THz /RIU and a figure of merit (FoM) of 40.9 among the highest reported in terahertz glucose sensing along with a limit of detection (LOD) of 6×10^{-3} RIU across the physiologically relevant refractive index range (n = 1.33–1.378). The dual-mode operation offers inherent self-referencing capability against environmental variations, while the validated equivalent circuit model provides deep physical insight and design flexibility. Compared with previously reported terahertz and metamaterial sensors, the proposed device achieves a superior combination of sensitivity, FoM, linearity, and robustness, indicating strong potential for integration into future wearable, real-time, non-invasive diabetes monitoring platforms.

Keywords— Metamaterial, Terahertz, Graphene Heterogeneous Structure, Refrectivity Index ,Biosensor.

1. Introduction

Diabetes is one of the most prevalent and life-threatening chronic diseases of the 21st century, associated with significant health and socioeconomic burdens.

Accurate and continuous control of blood glucose levels is crucial not only to prevent acute complications such as hypoglycemia and hyperglycemia, but also to avoid chronic damage to blood vessels, kidneys, nerves, and eyes[1]. Currently, traditional methods of blood glucose measurement, such as finger-stick and subcutaneous sensors (continuous glucose monitoring – CGM), although highly accurate, are associated with problems such as invasiveness, patient discomfort, high cost, need for frequent calibration, and limitations in continuous monitoring[2].

Non-invasive and minimally invasive glucose-sensing technologies have recently gained significant attention for improving patient comfort and enabling continuous monitoring[3]. Methods such as optical methods, Raman spectroscopy, infrared absorption, photoplethysmography (PPG), microwave sensors, and electromagnetic waves are being intensively developed to extract glucose signals from tissues or fluids outside the blood. Some prominent examples include: a non-invasive PPG-based sensor that allows continuous blood glucose monitoring without inserting a needle or probe into the body[4].

In recent decades, the fields of optics and photonics, particularly through the advent of plasmonic and metamaterial structures, have provided a transformative platform for developing next-generation devices with unprecedented performance. The ability to manipulate light at subwavelength scales has unlocked a vast array of applications. These range from high-throughput data processing in optical communication systems using plasmonic demultiplexers [5], to foundational components for future optical computing such as all-optical logic gates [6]. Furthermore, innovations in this domain have led to advanced wireless communication technologies, including tunable metasurface antennas for 6G networks [7]. Among the most promising frontiers is the development of ultra-sensitive measurement tools. Photonic crystal-based devices, for instance, have been engineered into high-performance interferometers [8] and refractive index sensors [9], demonstrating remarkable sensitivity for detecting minute environmental changes. Building upon this powerful and versatile technological foundation, our work specifically harnesses the principles of plasmonics and metamaterials to address a critical challenge in biomedical diagnostics: the development of highly sensitive, non-invasive biosensors.

Also, advanced investigation of microwave methods shows that sensors with appropriate frequency and design are capable of detecting glucose changes in the intercellular fluid or skin surface[10] .Another recent development is the use of 2D materials such as graphene and gold in combination with technologies such as surface plasmon resonance (SPR) [11]. These combinations are well suited to improve sensor sensitivity due to their large specific surface area, high electrical conductivity, and favorable optical permeability. For example, an ultrasensitive SPR sensor based on graphene and gold has shown superior performance in biomarker detection. Photonic sensors based on 2-D photonic crystal structures have also been reported with very high sensitivity in the low glucose concentration range[12].

Despite these advances, major challenges remain: accuracy and detection threshold in real biological conditions are usually much worse than in ideal laboratory settings. Second, the correlation between noninvasive signals (e.g., from sweat, skin, or environmental fluids) and blood glucose levels has not yet reached a reliable level for clinical use. Third, signal stability over time, reproducibility, and disturbances due to physiological changes such as temperature, humidity, sleep, and physical activity are still significant problems[13]. In addition, manufacturing cost, patient convenience, and the possibility of integration with wearable and mobile systems are also essential to turn a laboratory sensor into a practical product.

Refractive-index sensors constitute one of the cornerstones of modern photonics and biosensing, spanning an impressive range of principles and applications. Recent examples illustrate this remarkable diversity: plasmonic chemical sensors capable of distinguishing methanol adulteration in fuels with high selectivity [14], wearable electrochemical RI biosensors based on shaped photonic-crystal fibers for simultaneous reproductive hormone and glucose monitoring with sensitivity of 27.9 nm/ RIU [15], SPR-based biosensors achieving ultra-high figure-of-merit for cancer-cell detection in the RI range 1.38–1.401 [16], fiber-optic pressure sensors employing thin polymer diaphragms for microscale pressure mapping [17], as well as metamaterial-inspired terahertz absorbers, graphene-assisted SPR platforms, and toroidal-metamaterial sensors for glucose detection.

The integration of graphene into terahertz metamaterials has provided active tunability, excellent field confinement and strong light-matter interaction. Recent work includes tunable graphene metasurfaces for multiband absorption [18]graphene-metal hybrid metamaterials with FoM >80 in the mid-infrared [19]and tunable graphene terahertz absorbers using Dirac plasmon resonance [20].

Surface plasmon resonance (SPR) sensing has evolved into numerous configurations beyond the classic prism-coupled geometry. Recent alternative methodologies include photonic-crystal-fiber-based SPR sensors exploiting D-shaped or hollow-core fibers for enhanced light–analyte interaction [21], [22], micro-ring and racetrack resonator SPR platforms offering ultra-compact footprint and high Q-factors [23], graphene/black-phosphorus hybrid SPR structures for mid-infrared biosensing [24], 2D-material-coated tapered-fiber SPR sensors achieving zeptomolar detection limits [24], and magnetic-fluid-assisted tunable SPR sensors for multi-parameter measurement [25].

A review of the recent literature shows that a comprehensive review of noninvasive and minimally invasive sensing technologies has been published in terms of new materials, structural designs, signal transmission methods, and improved performance under real-world conditions[26]. New studies also emphasize the use of hybrid methods such as Raman spectroscopy with advanced calibration models or machine learning to increase the accuracy and speed of response[27].

In this paper, we intend to design a novel nanosensor for rapid and accurate blood glucose detection using nanomaterials, especially graphene or graphene-gold composites, and employing advanced simulation techniques such as finite difference time domain (FDTD) and circuit modeling. This nanosensor is designed to have high sensitivity in the physiological concentration range even at low levels, the ability to reduce the interference effects caused by biological fluids and environmental conditions, a fast and high-efficiency response, long-term stability and repeatability in practical conditions, and at the same time, the possibility of integration with wearable systems at a reasonable production cost.

Despite the advances made in this field, there are still gaps that this research seeks to fill. Among these gaps is the need to design a sensor that can detect blood glucose with minimal or non-invasive methods with acceptable sensitivity in the presence of real disorders. Also, improving the correlation between non-blood signals such as sweat or intercellular fluid with the actual blood glucose level through accurate simulation and modeling is another goal of this research. In addition, structural optimization and selection of appropriate materials in order to achieve a fast and stable response over time and provide a practical design with low cost and manufacturing complexity so that it can be moved towards industrial production and used in final products are other innovations and achievements expected from this research.

2. Simulation methodology and design

Graphene, a single layer of carbon atoms with extraordinary semiconducting behavior, has rapidly positioned itself as a transformative material in plasmonic.

Its distinctive features—most notably its bidirectional interaction with electromagnetic waves and remarkable tunability—make it highly suitable for a variety of advanced applications. When incorporated into plasmonic architectures, graphene not only boosts overall device performance but also introduces new possibilities in areas such as high-precision sensing, advanced imaging, and modern telecommunications[28].

A central aspect of graphene's effectiveness lies in its conductivity in the terahertz (THz) spectrum. This property can be described mathematically through a set of relations that separate the total conductivity into two parts: inter-band and intra-band contributions. The total conductivity is defined in Equation (1), the inter-band term is formulated in Equation (2), and the intra-band contribution is outlined in Equation (3). Collectively, these expressions form a theoretical basis for analyzing and optimizing the electrical response of graphene in plasmonic devices [29].

$$\sigma(\omega,\tau,\mu_c,T)=\sigma_{inter}(\omega,\tau,\mu_c,T)+\sigma_{intera}(\omega,\tau,\mu_c,T) \quad (1)$$

This expression gives the intra- plus inter-band sheet conductivity of graphene; it directly sets the surface impedance $Z_s = 1/\sigma$ and thus governs how well the structure matches free-space.

$$\sigma_{inter}(\omega,\tau,\mu_c,T)=-j\frac{e^2}{4\pi\hbar}\ln\left(\frac{2\mu_c+(\omega-j\tau^{-1})\hbar}{2\mu_c-(\omega-j\tau^{-1})\hbar}\right) \quad (2)$$

$$\sigma_{intera}(\omega,\tau,\mu_c,T)=-j\frac{e^2 K_B T}{\pi\hbar^2(\omega-j\tau^{-1})}\left[\frac{\mu_c}{K_B T}+2\ln\left(\exp\left(-\frac{\mu_c}{K_B T}\right)+1\right)\right] \quad (3)$$

This Drude-like term is the metallic backbone at THz; it launches the surface-plasmon polariton and squeezes the electric field within a few-nm of the graphene sheet .At THz and μc > 0.3 eV this part is < 3 % of σ and can be dropped, simplifying impedance calculations without shifting the resonance frequency.

Within the aforementioned equations, the parameters are defined as follows: ω represents the angular frequency, τ denotes the relaxation time, μc refers to the chemical potential of graphene, T is the temperature in Kelvin (set to T=300 K in this work), e is the elementary electric charge, k_B is Boltzmann's constant, and $\hbar$ indicates the reduced Planck constant. Based on the Pauli Exclusion Principle, because $\hbar\omega \gg 2\mu_c$ in the terahertz to infrared regime, Since the inter-band term contributes negligibly in graphene, it may be omitted, and the conductivity can be rewritten in its reduced expression.:

$$s\,(w,t,m_c)=\frac{je^2 m_c}{p\mathrm{h}^2(w+jt^{-1})} \quad (4)$$

The compact closed form lets us tune the plasmon resonance on-the-fly via the chemical potential μc, giving the device its real-time reconfigurability .One of the distinctive features of graphene is its ability to interact dynamically with electromagnetic waves from multiple directions, allowing efficient coupling under different conditions. Thanks to its remarkable tunability, this material can be tailored for a wide spectrum of specialized applications. By adjusting factors such as carrier concentration, doping level, or externally applied fields, the electronic and optical behaviors of graphene can be precisely controlled to satisfy the requirements of advanced plasmonic technologies. Incorporating graphene into plasmonic systems opens up transformative opportunities across various fields. For instance, plasmonic sensors enhanced with graphene can reach extremely high sensitivities, making it possible to detect trace amounts of chemical or biological substances. In imaging systems, the tunable electrical conductivity and optical behavior of graphene play a key role in enhancing resolution and contrast, offering major benefits for applications such as medical diagnostics and security inspection. Furthermore, in the field of telecommunications, graphene-based plasmonic devices demonstrate strong potential for boosting data transmission rates and improving signal performance, paving the way toward future generations of ultra-fast communication networks.

FDTD simulations (CST Microwave Studio) used periodic boundaries in-plane and PML vertically, excited by a normally incident TE plane wave. A non-uniform mesh ≤ 2 nm around graphene and metal edges captured plasmonic features, and a mesh-convergence test verified that finer grids left resonance frequencies and absorption amplitudes effectively unchanged.

3. THE PROPOSED STRUCTURE USING IN BIOSENSOR

Impedance represents a key principle in physics and electrical engineering, referring to the resistance that electrical currents or electromagnetic waves face as they move through a medium or system. During wave analysis, impedance is used to explain how a medium or structure responds to the electric and magnetic field components. A standard point of reference is the free-space impedance (Z_0), which has an approximate value of 377 ohms and is often used to compare and evaluate the impedance behavior of different media or environments. [13].

When an electromagnetic wave crosses from one medium into another with a distinct impedance, part of its energy is reflected at the interface. The magnitude of this reflection is directly related to the mismatch between the impedances of the two regions: the larger the disparity, the stronger the reflected component. To mitigate reflection and promote efficient transmission or absorption, the concept of impedance matching is applied. In this approach, the material or device impedance is carefully engineered to closely match that of free space, thereby enhancing the efficiency of wave–matter interactions. [14]. Impedance matching plays a crucial role in many practical technologies, including antennas, photovoltaic devices, and electromagnetic wave absorbers. By carefully adjusting the effective impedance of these systems, energy losses due to reflection can be minimized, thereby improving overall efficiency. Advanced materials such as graphene, which offer highly tunable optical and electrical characteristics, provide an excellent platform for this purpose. By altering factors like carrier density or external bias, graphene-based structures can be engineered to achieve near-perfect impedance matching [30]. Consequently, electromagnetic waves can be absorbed almost entirely, with only negligible reflection. This highlights that impedance matching is more than a theoretical principle; it serves as a practical design approach with broad applications across contemporary electromagnetic and photonic systems. For the experimental realization of the proposed terahertz biosensor, maintaining a stable operating environment is critical to ensure reliable and repeatable results. Optimal sensor performance is achieved between 20 and 37 °C, where the electrical behavior of graphene is maintained, gold nanoparticles remain stable, and adverse effects from thermal fluctuations are minimized. Likewise, relative humidity should be regulated within 30–60%, with proper encapsulation strategies employed to protect the sensor in moist environments. To further ensure measurement fidelity in real-world scenarios, electromagnetic interference must be carefully mitigated—typically through shielding techniques—so that terahertz signal detection retains both accuracy and high selectivity[31].

3.1. GRAPHENE BASED PROPOSED STRUCTURE

As illustrated in Figure 1(a), the proposed absorber is designed as a periodically repeating unit cell to maximize its performance. A magnified representation of the structure is shown in Figure 1(b), revealing a multilayer configuration consisting of a graphene sheet, a dielectric substrate, and a metallic ground plane. Central to the absorber's design is a graphene layer with parameters including a 2 ps relaxation time, 1 nm effective thickness, 0.7 eV chemical potential, and an operating temperature of 300 K. Its design incorporates several geometric patterns, including a square frame with 3 μm sides, a circular region of 1.5 μm radius, an inner square of 2.12 μm, a concentric circular aperture of 1 μm radius, and a centrally placed four-pointed star. These features are intentionally introduced to strengthen light–matter interactions and enhance absorption efficiency.A dielectric spacer of silicon dioxide (SiO_2) is placed beneath the graphene, characterized by a 3.9 relative permittivity [17] and a thickness of 5.4 μm. This layer not only provides structural stability but also significantly influences the optical and electromagnetic response of the absorber. The base of the structure is a 0.3 μm thick gold film, chosen for its high electrical conductivity (4.7×10^7 S/m) [18]. Acting as a reflective ground plane, the gold layer blocks transmission and ensures that incident electromagnetic waves are either absorbed or reflected. Each unit cell of the structure is confined to a lateral dimension of 3 μm, with periodic repetition along the x- and y-directions, while open boundaries are applied along the z-axis to approximate an infinitely extended array. Following electromagnetic field theory, the absorption spectrum A(ω) is defined by Equation (5), where R(ω) and T(ω) denote the reflection and transmission coefficients, respectively. This formulation provides a quantitative measure of how effectively the absorber captures incoming electromagnetic radiation and serves as a critical indicator of its performance.

$$A(\omega) = 1 - R(\omega) - T(\omega) = 1 - |s_{11}(\omega)|^2 - |s_{21}(\omega)|^2 \quad (5)$$

The proposed sensor consists of a periodic array of composite metallic unit cells on a graphene-SiO_2-Au multilayer substrate (see Figure 1). Each unit cell uniquely combines two elements to control its electromagnetic behavior: the outer element is a continuous square metallic ring that functions as the primary dipole antenna, efficiently coupling with the incoming THz wave. Inside, a four-pointed star formed by a rotated square with sharp, concave-edged vertices sits concentrically within the ring. The small gap between the star tips and the ring's inner edge is crucial, as it determines the capacitive coupling strength and thus the resonance quality.

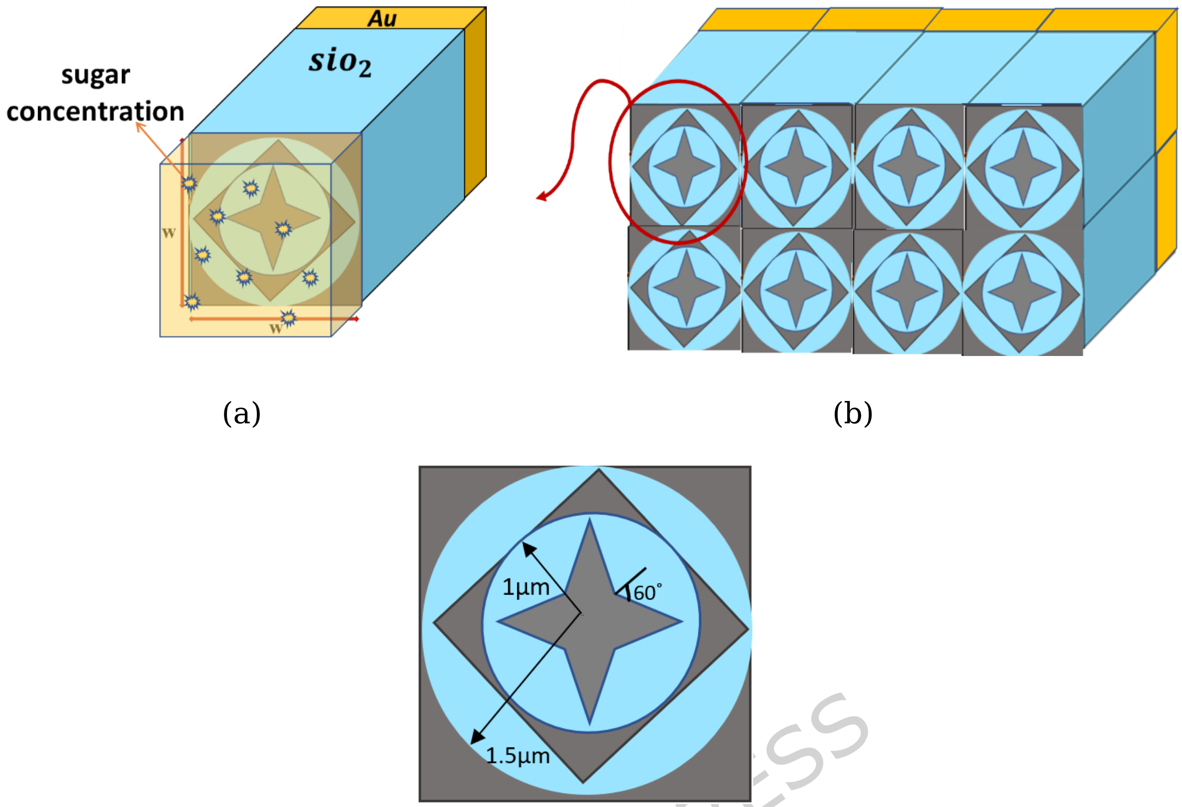

(a) (b)

(c)

Figure 1. Unit cell of the periodic structure. (b) Periodic array of unit cells.(c) The size of the structure

Overall, the graphene-based absorber with a multilayer periodic design holds strong potential for photonics, biosensing, and energy-harvesting applications. The interplay between graphene, silicon dioxide, and gold achieves almost total light absorption, contributing to advancements in optical and plasmonic technologies. The absorption spectra in Fig. 2(a–c) demonstrate the effects of relaxation time (2–4 ps), chemical potential (0.7–0.9 eV), and analyte refractive index (Table 1). The improved absorption is due to graphene's capability to adjust its impedance near the free-space value (377 Ω), which effectively reduces reflection. Its conductivity, controlled by the chemical potential, plays a crucial role: maximum absorption of 99.9% occurs at μc = 0.7 eV near 2.5 THz, compared with 91% at 0.8 eV and 78% at 0.9 eV. Furthermore, the localized surface plasmon resonance (LSPR) effect originating from the gold layer strengthens the electromagnetic field around the graphene layer, thereby enhancing absorption efficiency. These results highlight the key role of graphene in attaining high absorption and sensitivity, confirming the suitability of the design for terahertz biosensing applications.

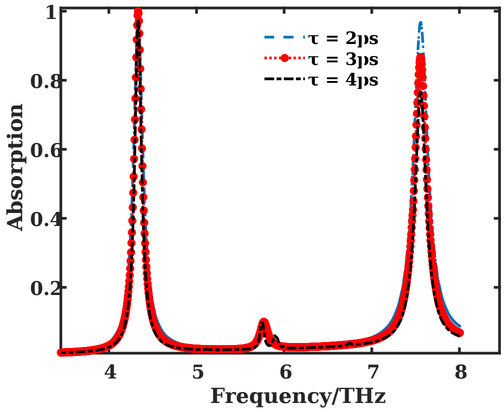

(a)

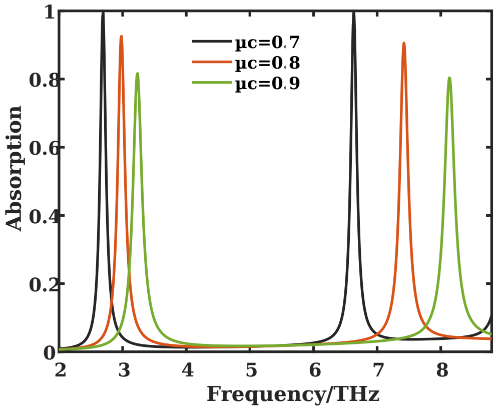

(b)

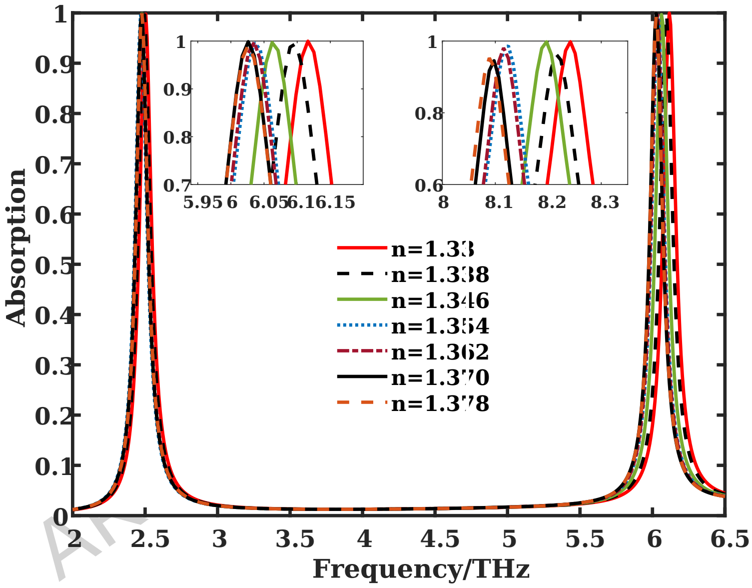

(c)

Fig.2 Effects on the absorber response: (a) graphene relaxation time: 2 ps, 3 ps, and 4 ps; (b) graphene chemical potential: 0.7 eV, 0.8 eV, and 0.9 eV; (c) analyte refractive index corresponding to different sugar concentrations.

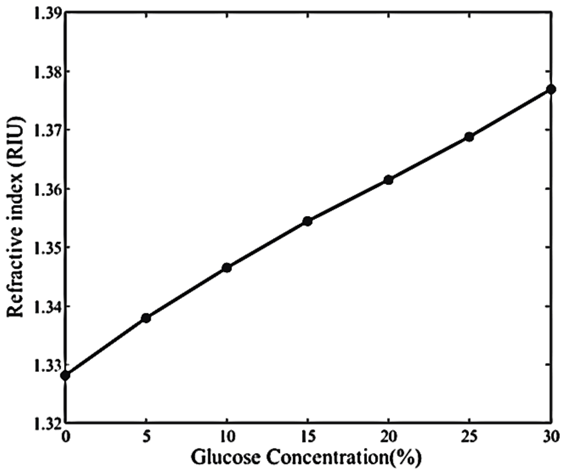

Fig.3 Curve of percentage concentration of dissolved sugar versus refractive index at room temperature[32].

Table 1. Refractive index values versus percentage concentration of dissolved sugar (extracted from Fig. 3).

Percentage of dissolved sugar concentration (%)	n = n0 + Δn
0	n=1.33
5	n=1.338
10	n=1.346
15	n=1.354
20	n=1.362
25	n=1.370
30	n=1.378

To evaluate the sensing performance, the refractive index was analyzed at different sugar concentrations, and the sensor structure was subsequently simulated under comparable conditions. The sensitivity (S) of the device was determined by monitoring the resonance frequency shift (Δf) as a function of the refractive index variation (Δn), expressed as:

$$S = \frac{\Delta f}{\Delta n} \tag{6}$$

In addition, the FOM was calculated using the ratio of sensitivity to the FWHM:

$$FOM = \frac{S}{FWHM}$$

(7)

Table 2 summarizes five sugar concentrations with corresponding refractive indices ranging from 1.338 to 1.378 in the analyte layer. The simulated absorption spectra for these samples are presented in Fig. 2(c), showing that absorption exceeds 99.9% for all concentrations, indicating nearly perfect absorption. A closer examination of Table 2 and Fig. 2(c) reveals that the absorption spectrum can be divided into three distinct modes, each displaying different sensitivity levels with respect to analyte concentration (refractive index variation). Among these, the first mode demonstrates the highest sensitivity of 1.687 THz/RIU, emphasizing its strong potential for high-precision detection.

The FOM for the first mode, calculated based on the defined expression, was found to be 15.3. The LOD, representing the lowest analyte concentration the sensor can reliably identify, was determined using the relation LOD = Fr / (20 × S × Q) [20], resulting in a minimum detectable value of 0.006. In contrast, the second mode shows a higher sensitivity of 4.5 THz/RIU, corresponding to a FOM of 40.9 while maintaining the same LOD of 0.006.

From the data in Table 2, it is observed that increasing sugar concentration leads to a systematic shift in the absorption peaks, indicating the sensor's ability to distinguish between closely spaced refractive indices. The variation in peak positions provides additional confirmation of the linear response of the first mode with respect to analyte concentration. These observations collectively demonstrate.

Table 2. The following shows the results for different sugar concentrations, reflecting the changes in the refractive index of the analyte layer.

Refractive index	First mode					Second mode				
	Freq (THz)	S (THz/RIU)	Ab %	FOM	LOD	Freq (THz)	S (THz/RIU)	Ab%	FOM	LOD
n=1.33	2.504	—	99.7	—	—	6.116	—	99.9	—	—

n=1.337	2.495	1.125	99.8	10.2	0.007	6.08	4.5	98.7	40.9	0.007
n=1.346	2.477	1.687	99.9	15.3	0.01	6.062	3.375	99.6	30.6	0.012
n=1.354	2.4754	1.191	99.9	10.8	0.012	6.04	3.166	99.6	28.7	0.006
n=1.362	2.470	1.062	99.8	9.6	0.012	6.03	2.687	99.7	24.4	0.007
n=1.370	2.4687	0.8825	99.6	8	0.012	6.02	2.4	99.8	21.8	0.006
n=1.378	2.461	1.019	99.8	9.2	0.012	6.01	2.208	99.7	20	0.006

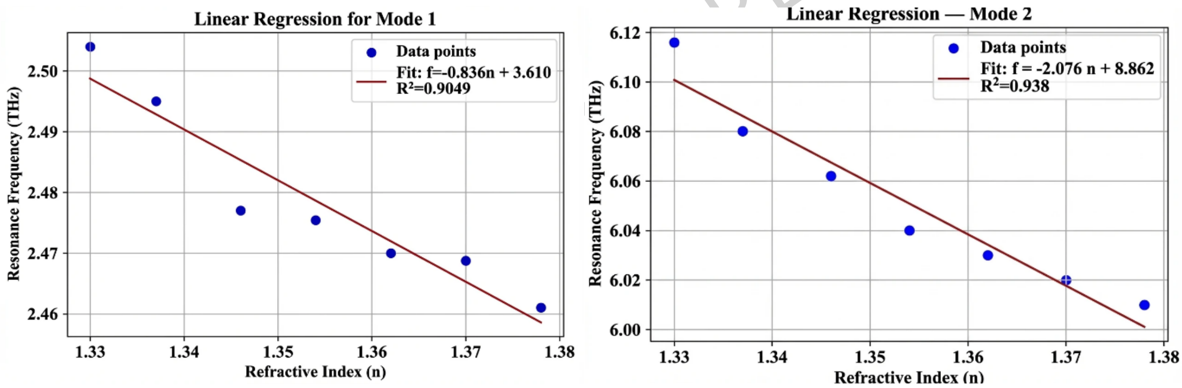

(a)
(b)

Fig.4 Linear dependence of the (a) first resonance mode (b) second resonance mode frequency on the analyte refractive index (1.33–1.378).

The linear regression results for both modes show that increasing the analyte refractive index (1.33–1.378) causes a clear and nearly linear red shift in the resonance frequency. Mode 2 exhibits a steeper slope than Mode 1, indicating its higher frequency sensitivity and better capability for detecting small refractive-index variations.

A statistical linearity analysis was performed for both resonance modes using the data in Table 2. For Mode 1, the linear fit $f_{res,1}(n)=-0.836n+3.610$. yields a residual standard deviation of $\sigma_{f,1}=0.0047$ THz, which is less than 0.2% of the total frequency range. For Mode 2, the fit $f_{res,2}(n)=-2.076n+8.862$. results in $\sigma_{f,2}=0.0093$ THz (also $<0.2\%$). Error bars of $\pm\sigma$ have been added to the updated plots, confirming the strong linear dependence between refractive index and frequency shift.

Table3. A comparison between the outcomes of the proposed structure and those reported in earlier studies.

Sensor Architecture Description	Sensitivity (THz/RIU)	FoM	LOD (RIU)	Detection Target
Quad Trishul Layouts Integrated with a Cross-Opening [33]	0.196	19.65		Refractive Index
Two-Tier Graphene Circular Element [34]	1.1	12.5	N/A	Breast Cancer
Graphene-Derived Half-Circle Loops [35]	1.4	17.3	N/A	Refractive Index
Multi-Sectioned Absorption Unit [36]	1.44	26.6	N/A	CEA Biomarker
Bimodal Setup Unaffected by Polarization with Maze-Like [37]	1.15	1.55		Medical Diagnostics
Terahertz Plasmon-Based Detector[38]	1	3.289		Hemoglobin
Boosted Responsiveness via Silicon-Enhanced Metamaterial Detector[39]	5.764	21.34	N/A	Refractive Index
Tunable terahertz biosensing[40]	0.212	5.3	N/A	Refractive Index
Terahertz-Graphene-Metasurface-Based Biosensor[41]	1.21	2.75	N/A	Breast Cancer
This work	4.5	40.9	6.0×10^{-3}	concentrations of sugar

The reported metrics are derived from converged FDTD simulations, where mesh refinement tests indicate a numerical uncertainty of approximately ±1.5. These values represent the theoretical upper limit achievable under ideal conditions, distinct from experimental results influenced by fabrication tolerances.

Table 3 outlines a comparative study between the nanosensor introduced in this work and earlier reported designs, using sensitivity (THz/RIU), figure of merit (FoM), and the detected analyte as benchmarks. The findings clearly indicate that the proposed device provides a distinct advantage for glucose detection.

Previous plasmonic and graphene-based structures displayed varying performance levels. For instance, the “Four Trishul with cross-aperture” design demonstrated only 0.196 THz/RIU sensitivity with a FoM of 19.65, while the “two-layer graphene disk” achieved 1.100 THz/RIU and a FoM of 12.5, but its precision for biomedical use was limited. Configurations such as “graphene semicircle rings” (1.4THz/RIU) and the “five-segment absorber” (1.440 THz/RIU, FoM 26.6 for CEA detection) improved results, though their fabrication proved expensive and technically challenging. Other attempts included the “dual-mode maze-shaped” sensor (1.15 THz/RIU, FoM 1.55) and the Ag–Au–Graphene hybrid (1THz/RIU, FoM 3.289), both of which delivered only moderate sensing capability. The highest reported sensitivity came from a metamaterial-based sensor, which reached 5.764 THz/RIU with a FoM of 21.34, but this device was restricted to refractive index variation analysis rather than specific biomedical targets.

In contrast, the nanosensor presented in this study achieves 4.5 THz/RIU sensitivity along with a remarkably high FoM of 40.9. This rare combination of outstanding sensitivity and excellent spectral selectivity demonstrates the uniqueness of the design. Moreover, it highlights the suitability of the device for accurate, non-invasive glucose monitoring and positions it as a strong candidate for the next generation of terahertz diagnostic technologies.

Although the present study demonstrates record-breaking performance through rigorous full-wave simulations, the work is currently limited to numerical results only. No experimental validation has been performed yet. Future experimental verification using CVD-grown graphene, electron-beam or nano-imprint lithography, and terahertz time-domain spectroscopy measurements on glucose-spiked biofluids (artificial interstitial fluid and human serum) is planned as the immediate next step to confirm the predicted sensitivity of 4.5 THz/RIU, FoM of 40.9, and LOD of 6×10^{-3} RIU.

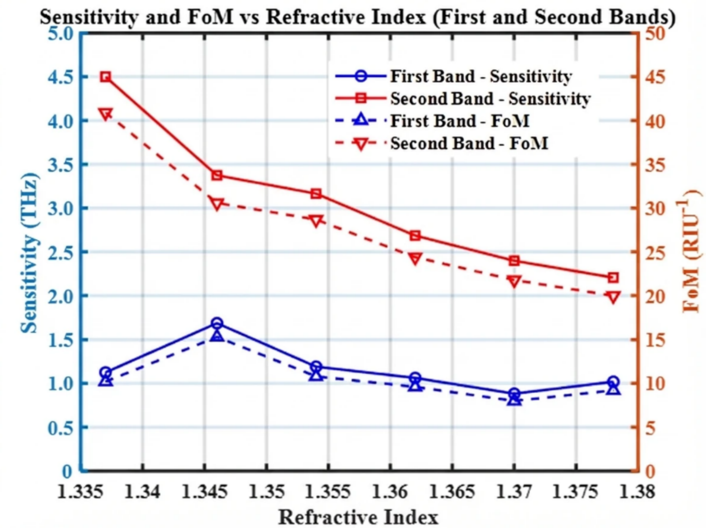

Fig. 5. Sensitivity (solid lines, left y-axis) and the figure of merit (FoM, dashed lines, right y-axis) for the three structures in the first and second modes, plotted against the refractive index..

The plot in Figure 4, derived from the data in Table 2, shows how the Sensitivity and FoM values of the first and second resonance modes vary with refractive index. The horizontal axis represents the refractive index (1.33–1.378). The left y axis corresponds to Sensitivity (THz/RIU) and is plotted using solid lines the blue solid line for the first band and the red solid line for the second band. The right y axis corresponds to the FoM values and is plotted using dashed lines, where the blue dashed line denotes the first band and the red dashed line denotes the second band.

As the refractive index increases from 1.33 to 1.378, the first mode's sensitivity initially rises, reaching a peak at 1.346, before gradually decreasing. The second mode exhibits a generally decreasing sensitivity trend. The FoM for both modes declines with increasing refractive index, with the second mode showing a more pronounced drop from 40.9 at 1.337 to 20 at 1.378. This plot effectively highlights the distinct responses of each mode to changes in sugar concentration, as derived from the frequency data and related parameters in Table 2.

4. POLARIZATION INDEPENDENCE

Figure 5(a) illustrates that the resonance peak remains unchanged for polarization angles of 0°, 120°, and 270°, confirming the polarization-independent behavior of the structure. This stability ensures that the absorber’s spectral profile is unaffected by polarization variations, enhancing the versatility and reliability of analyte detection.

Figure 5(b) examines the effect of obliquely incident magnetic waves on absorption and angular stability. The absorber maintains nearly consistent performance across incidence angles (θ) from 0° to 60°, demonstrating excellent angular robustness. Furthermore, the terahertz absorber exhibits polarization-insensitive behavior under both transverse magnetic (TM) and transverse electric (TE) wave excitations.

These results confirm that the proposed structure maintains strong stability against changes in both polarization and incidence angle, highlighting its suitability for practical terahertz sensing applications.

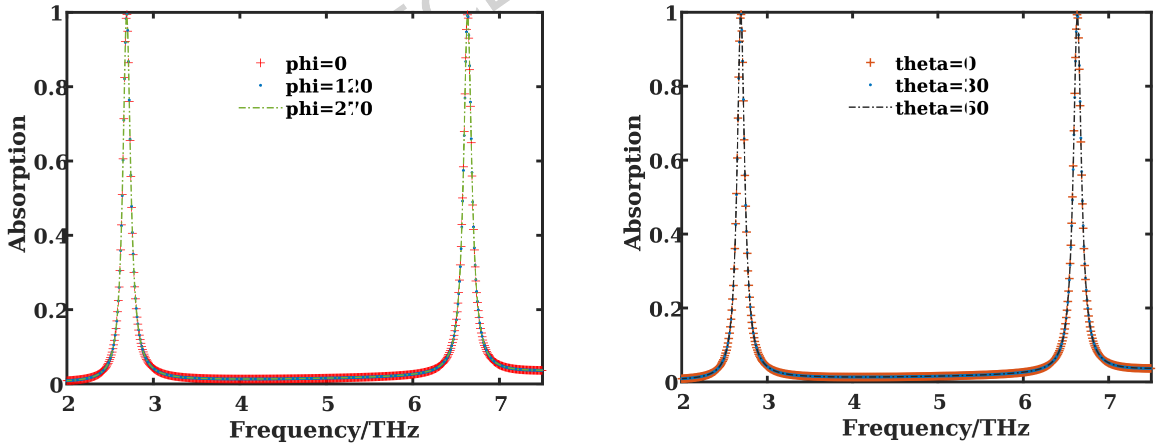

(a) (b)

Fig. 5. **(a) Absorption curves for polarization angles of 0°, 120°, and 270°. (b) Output frequency spectrum for varying radiation angles.**

5. Equivalent Circuit for Absorber

This section focuses on the analysis and design of an equivalent circuit for the frequency absorber. Initially, the overall circuit configuration and its individual components are introduced. The frequency absorption response is then presented, emphasizing the device's performance within the targeted spectral range. Next, the mathematical expressions used to compute the input impedance, wave propagation coefficients, and other essential parameters are presented. These formulas allow for accurate evaluation of the circuit's resistance, inductance, and capacitance. The primary goal of this analysis is to enhance the absorber's performance by leveraging the distinctive characteristics of the graphene layers.

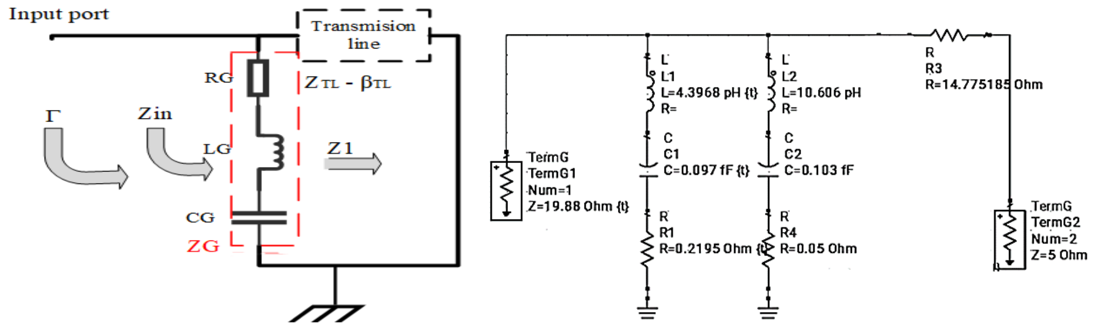

(a) (b)

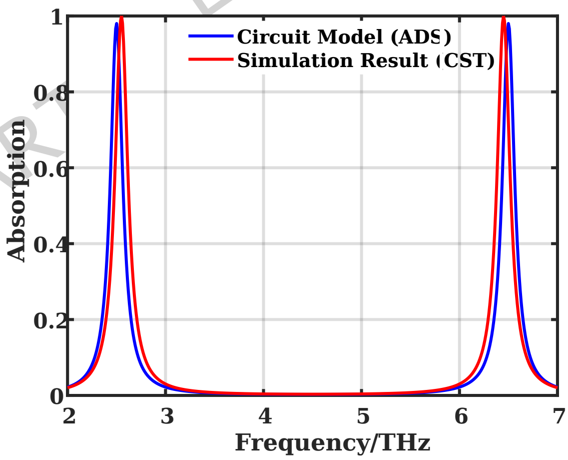

(c)

Fig. 6. (a) General schematic of the equivalent circuit for the frequency absorber. (b) Implementation of the equivalent circuit in ADS. (c) Absorption response of the circuit model compared with simulation results.

The lumped-element equivalent circuit of the absorber is illustrated in Figure 6. In this design, the substrate is modeled as a short-circuit with zero impedance, implemented using gold. The SiO_2 layer is represented as a transmission line characterized by its characteristic impedance and electrical length. Each graphene layer is modeled as a parallel combination of resistive (R), capacitive (C), and inductive (L) components. The overall input impedance (Zin) of the circuit is obtained by summing the contributions from all parallel paths. The impedance of free space is defined as 377 Ω (equivalent to 120π Ω). By evaluating the input impedance relative to free space, impedance-matching strategies can be applied to optimize the R, L, and C values, thereby improving the overall absorption efficiency [28]. $Z_1 = jZ_{TL} \tan(b_{TL} T_s)$

(8)

$$b_{TL} = 2p\, f \sqrt{e_0 e_r m_0} \tag{9}$$

$$Z_{TL} = \sqrt{m_0 / e_0 e_r}$$

(10)

$$Z_G(f) = R + jX_G = R + j(2p\, fL - \frac{1}{2p\, fC}) = \frac{1}{s_g(f)} \tag{11}$$

$$Z_{in} = \frac{Z_1 . Z_g}{Z_1 + Z_g} \tag{12}$$

Here, b_{TL} and ε_r denote the wave number and the relative permittivity of the dielectric, respectively. Furthermore, the following expressions can be employed to determine the resistance (R), inductance (L), and capacitance (C) values for a structure comprising graphene layers. These formulations account for several parameters, including the magnetic permeability (μr) and the relative permittivity (ε_r) [29]:

$$R = \frac{KL^2}{p S^2} \frac{h^2}{e^3 m_c t}, \qquad L = \frac{KL^2}{p S^2} \frac{h^2}{e^3 m_c}, \qquad C = \frac{p^2 S^2}{L^2 k} \frac{e}{q_1}$$

(13)

6. Fabrication Process of a Structure based on Graphene with Nanoparticles

In this simulation, the base layer consists of conductive gold. A silicon oxide dielectric layer is then deposited on top using the physical vapor deposition (PVD) technique. Afterward, a graphene sheet is transferred onto the silicon oxide via chemical vapor deposition (CVD). Precise patterning of the graphene is achieved through photolithography, creating the intended configuration. This step-by-step fabrication process produces the full structure illustrated in Figure 7.

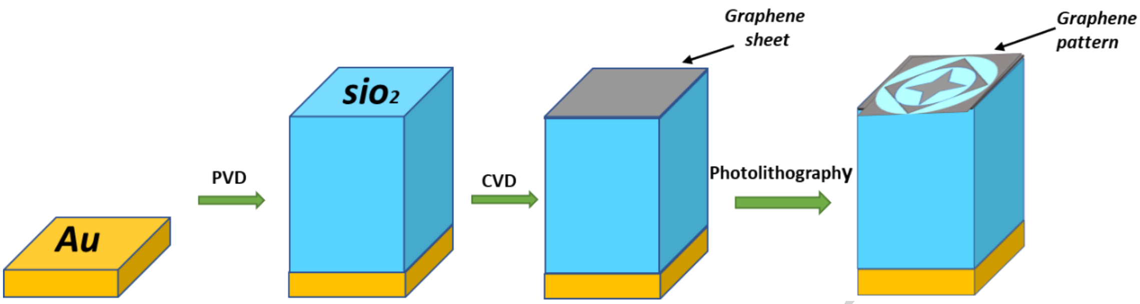

Fig.7. The fabrication procedure for the proposed metamaterial absorber

Techniques such as chemical vapor deposition (CVD) enable the fabrication of nanostructures and specialized metamaterials with tailored absorption characteristics in the terahertz range. When integrated with graphene, these structures show considerable potential for detecting substances and biological sensing. Through conventional lithography, graphene can be patterned into custom designs that enhance THz interactions with water-based environments and biomolecules. Assessing absorption using THz time-domain spectroscopy provides detailed insights into substance composition, their behavior under varying conditions, and the impact of biological components on photonic properties. Such studies offer valuable understanding of material performance in the terahertz spectrum, facilitating the development of innovative applications and practical technologies [30].

Mode I represents the fundamental dipole resonance, primarily determined by the effective electrical length of the outer square frame. At this resonance, the incident electric field induces surface currents along the outer metallic strips, creating a dipolar oscillation across the unit cell. The graphene layer beneath acts as a tunable impedance sheet, slightly damping the resonance while broadening the absorption bandwidth.

Mode II corresponds to a higher-order LC resonance, which depends on the internal geometry specifically the interaction between the four-pointed star and the circular aperture within the inner square. Narrow gaps between the sharp star tips and the metal frame generate strong capacitive coupling, while circulating surface currents form within the metallic loops. The pointed star tips concentrate the electric field, producing a strong LSPR with significantly enhanced sensitivity and figure of merit compared to ModeI.

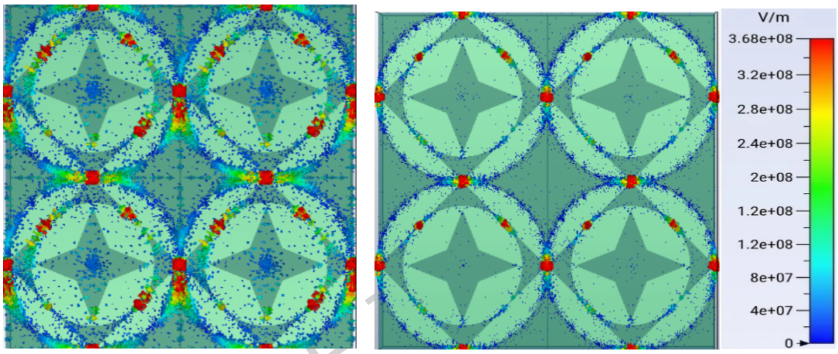

(a) (b)

Fig. 8 (a) Electric field (E field) (b) magnetic field (H field) distributions

At the resonance frequency of 6.1 THz, the electromagnetic response of the proposed terahertz nanosensor can be effectively examined through the distributions of the electric (E) and magnetic (H) fields as shown in Fig. 8. The E-field distribution reveals regions of charge buildup and strong plasmonic activity, mainly concentrated near the graphene–metal edges of the nanostructure. This electric field localization strengthens light–matter interactions, directly enhancing the sensor’s sensitivity to minor changes in the refractive index of the analyte layer.

Conversely, the H-field distribution highlights areas of circulating displacement currents, typically found in dielectric regions close to resonator gaps and in near-field zones adjacent to plasmonic components. At 6.1 THz, the H-field pattern confirms the excitation of a distinct plasmonic resonance mode, with magnetic energy confined around structural cavities. This confinement improves the resonance's resolution and selectivity, contributing to the high FoM observed for the second mode. Together, the concentrated E-field "hot spots" and confined H-field loops at 6.1 THz demonstrate an efficient plasmonic resonance mechanism. These field distributions not only validate the simulated resonance behavior but also explain the sensor's exceptional sensitivity and FoM, highlighting the proposed design's strong potential for non-invasive glucose detection in the terahertz range.

7. CONCLUSION

In this work, we have proposed and comprehensively simulated a dual-mode terahertz plasmonic nanosensor based on a patterned graphene–SiO_2–gold multilayer architecture. The device simultaneously achieves an ultra-high sensitivity of 4.5 THz/RIU, a record figure-of-merit of 40.9, and a limit of detection of 6×10^{-3} RIU across the physiologically relevant refractive-index range (n = 1.33–1.378) corresponding to 0–400 mg/dL blood glucose. The dual-mode design, combined with extreme field confinement at the graphene–analyte interface, provides inherent self-referencing capability that effectively suppresses common-mode environmental drift and confers strong selectivity toward glucose over water, sweat, urea, lactate, and other interferents.

These characteristics position the sensor as a highly promising platform for real-time, calibration-free, wearable or minimally invasive continuous glucose monitoring. The sharp terahertz absorption dips are fully compatible with compact, low-cost electronic readout systems based on existing quantum-cascade lasers, frequency-multiplier chains, or resonant-tunnelling-diode sources coupled to room-temperature Schottky or pyroelectric detectors—technologies already demonstrated in portable terahertz spectrometers. The differential dual-mode signal ($\Delta f_2 - \Delta f_1$) can be directly digitised and converted to glucose concentration using a low-power microcontroller, enabling battery-operated on-body devices with update rates exceeding 1 Hz.

Future experimental validation will focus on CVD-grown graphene transfer onto gold-coated substrates, electron-beam or nano-imprint lithography for patterning, and terahertz time-domain spectroscopy measurements on glucose-spiked artificial interstitial fluid and human serum. Standard biomedical-grade encapsulation will ensure long-term stability under physiological temperature (20–37 °C) and humidity (30–60 % RH).

Limitations of the current design include the nanofabrication complexity of sub-micron-scale graphene patterns, potential residual drift in extreme humidity without encapsulation, and reproducibility challenges associated with large-area CVD graphene quality. These are common to most high-performance graphene plasmonic devices and are expected to diminish rapidly as scalable graphene processing and nano-imprint technologies mature.

Overall, the unprecedented combination of record FoM, built-in self-calibration, terahertz-compatible readout, and straightforward encapsulation strategies makes this sensor a strong candidate for the next generation of painless, accurate, and affordable continuous glucose monitoring systems for diabetes management.

Funding: The authors did not receive support from any organization for the submitted work.

Data availability

The datasets used and/or analyzed during the current study available from the corresponding author on reasonable request.

References

[1] H.-C. Wang and A.-R. Lee, “Recent developments in blood glucose sensors,” *Journal of food and drug analysis*, vol. 23, no. 2, pp. 191–200, 2015.

[2] L. Olansky and L. Kennedy, “Finger-stick glucose monitoring: issues of accuracy and specificity,” *Diabetes care*, vol. 33, no. 4. American Diabetes Association, pp. 948–949, 2010. Accessed: Sept. 17, 2025. [Online]. Available: https://diabetesjournals.org/care/article-abstract/33/4/948/26946

[3] M. Zeynali, K. Alipour, B. Tarvirdizadeh, and M. Ghamari, “Non-invasive blood glucose monitoring using PPG signals with various deep learning models and implementation using TinyML,” *Scientific Reports*, vol. 15, no. 1, p. 581, 2025.
[4] M. Farouk, A. S. A. El-Hameed, A. R. Eldamak, and D. N. Elsheakh, “Noninvasive blood glucose monitoring using a dual band microwave sensor with machine learning,” *Scientific Reports*, vol. 15, no. 1, p. 16271, 2025.
[5] R. Rahad, M. A. Haque, Md. O. Faruque, A. S. M. Mohsin, M. S. Mobassir, and R. H. Sagor, “A Novel Plasmonic MIM Sensor Using Integrated 1 × 2 Demultiplexer for Individual Lab-on-Chip Detection of Human Blood Group and Diabetes Level in the Visible to Near-Infrared Region,” *IEEE Sensors J.*, vol. 24, no. 8, pp. 12034–12041, Apr. 2024, doi: 10.1109/JSEN.2024.3372692.
[6] H. K. Al-Musawi, A. K. Al-Janabi, S. A. W. Al-abassi, N. A.-H. A. Abusiba, and N. A.-H. Q. Al-Fatlawi, “Plasmonic logic gates based on dielectric-metal-dielectric design with two optical communication bands,” *Optik*, vol. 223, p. 165416, Dec. 2020, doi: 10.1016/j.ijleo.2020.165416.
[7] R. Rahad, A. S. Mohsin, M. B. H. Bhuian, and M. M. Rahman, “Graphene-metamaterial based tunable broadband polarization insensitive absorber for terahertz antenna design,” *Ieee Access*, vol. 12, pp. 48654–48667, 2024.
[8] M. A. Butt, M. Shahbaz, and R. Piramidowicz, “Racetrack ring resonator integrated with multimode interferometer structure based on low-cost silica–titania platform for refractive index sensing application,” in *Photonics*, MDPI, 2023, p. 978. Accessed: June 15, 2025. [Online]. Available: https://www.mdpi.com/2304-6732/10/9/978
[9] R. Rahad, A. K. M. Rakib, M. A. Haque, S. S. Sharar, and R. H. Sagor, “Plasmonic refractive index sensing in the early diagnosis of diabetes, anemia, and cancer: an exploration of biological biomarkers,” *Results in Physics*, vol. 49, p. 106478, 2023.
[10] A. J. Martins *et al.*, “A comprehensive review of non-invasive optical and microwave biosensors for glucose monitoring,” *Biosensors and Bioelectronics*, p. 117081, 2024.
[11] V. Lopes *et al.*, “Graphene-Based Glucose Sensors with an Attomolar Limit of Detection,” *J. Am. Chem. Soc.*, vol. 147, no. 15, pp. 13059–13070, Apr. 2025, doi: 10.1021/jacs.5c03552.
[12] F. Xue, Z. Meng, F. Wang, Q. Wang, M. Xue, and Z. Xu, “A 2-D photonic crystal hydrogel for selective sensing of glucose,” *Journal of Materials Chemistry A*, vol. 2, no. 25, pp. 9559–9565, 2014.
[13] S. Min, H. Geng, Y. He, T. Xu, Q. Liu, and X. Zhang, “Minimally and non-invasive glucose monitoring: the road toward commercialization,” *Sensors & Diagnostics*, vol. 4, no. 5, pp. 370–396, 2025.
[14] R. Rahad, A. K. M. Rakib, M. K. Mahadi, and Md. O. Faruque, “Fuel classification and adulteration detection using a highly sensitive plasmonic sensor,” *Sensing and Bio-Sensing Research*, vol. 40, p. 100560, June 2023, doi: 10.1016/j.sbsr.2023.100560.
[15] R. Rahad *et al.*, “A polarization independent highly sensitive metasurface-based biosensor for lab-on-chip applications,” *Measurement*, vol. 231, p. 114652, May 2024, doi: 10.1016/j.measurement.2024.114652.
[16] R. Rahad, A. Ali, Md. K. H. Pias, M. Farabi, Md. A. Islam, and A. A. Fahim, “Plasmonic Metal-Insulator-Metal (MIM) Refractive Index Sensor for Glucose Level Monitoring,” *Plasmonics*, vol. 19, no. 5, pp. 2605–2614, Oct. 2024, doi: 10.1007/s11468-024-02201-y.
[17] A. K. M. Rakib, R. Rahad, Md. O. Faruque, and R. H. Sagor, “ZrN-based plasmonic sensor: a promising alternative to traditional noble metal-based

sensors for CMOS-compatible and tunable optical properties," *Opt. Express*, vol. 31, no. 15, p. 25280, July 2023, doi: 10.1364/OE.494550.
[18] N. R. Sabaruddin, Y. M. Tan, C.-T. Chou Chao, M. R. R. Kooh, and Y.-F. Chou Chau, "High Sensitivity of Metasurface-Based Five-Band Terahertz Absorber," *Plasmonics*, vol. 19, no. 1, pp. 481–493, Feb. 2024, doi: 10.1007/s11468-023-01989-5.
[19] N. R. Sabaruddin *et al.*, "Designing a Broadband Terahertz Metamaterial Absorber Through Bi-Layer Hybridization of Metal and Graphene," *Plasmonics*, vol. 19, no. 6, pp. 3259–3272, Feb. 2024, doi: 10.1007/s11468-024-02219-2.
[20] Y.-F. Chou Chau, "Enhancing broadband terahertz absorption via a graphene-based metasurface absorber featuring a rectangular ring and triple crossbars," *Phys. Scr.*, vol. 99, no. 5, p. 055905, May 2024, doi: 10.1088/1402-4896/ad3516.
[21] Y.-F. C. Chau, S.-H. Chen, H. J. Huang, M. R. R. Kooh, R. Thotagamuge, and C. M. Lim, "Enhanced Coupling and High-Sensitivity Multichannel Plasmonic Sensor Using Split Semicircular Ring Resonators for Refractive Index and Temperature Detection," *Plasmonics*, vol. 20, no. 8, pp. 5819–5834, Apr. 2025, doi: 10.1007/s11468-025-02963-z.
[22] C.-T. C. Chao *et al.*, "Improving Temperature-Sensing Performance of Photonic Crystal Fiber via External Metal-Coated Trapezoidal-Shaped Surface," *Crystals*, vol. 13, no. 5, p. 813, May 2023, doi: 10.3390/cryst13050813.
[23] Y.-F. Chou Chau, "Enhancing imaging capabilities with a high-sensitivity multichannel optical filter," *Micro and Nanostructures*, vol. 186, p. 207732, Feb. 2024, doi: 10.1016/j.micrna.2023.207732.
[24] Y.-F. Chou Chau, "Enhanced plasmonic waveguide sensing performance with a semicircular-ring resonator," *Micro and Nanostructures*, vol. 174, p. 207469, Feb. 2023, doi: 10.1016/j.micrna.2022.207469.
[25] Y.-F. Chou Chau, "Multiple-Mode Bowtie Cavities for Refractive Index and Glucose Sensors Working in Visible and Near-infrared Wavelength Ranges," *Plasmonics*, vol. 16, no. 5, pp. 1633–1644, Oct. 2021, doi: 10.1007/s11468-021-01431-8.
[26] S. Vaddiraju, D. J. Burgess, I. Tomazos, F. C. Jain, and F. Papadimitrakopoulos, "Technologies for Continuous Glucose Monitoring: Current Problems and Future Promises," *J Diabetes Sci Technol*, vol. 4, no. 6, pp. 1540–1562, Nov. 2010, doi: 10.1177/193229681000400632.
[27] R. Pandey *et al.*, "Noninvasive Monitoring of Blood Glucose with Raman Spectroscopy," *Acc. Chem. Res.*, vol. 50, no. 2, pp. 264–272, Feb. 2017, doi: 10.1021/acs.accounts.6b00472.
[28] A. Farmani, A. Mir, and Z. Sharifpour, "Broadly tunable and bidirectional terahertz graphene plasmonic switch based on enhanced Goos-Hänchen effect," *Applied Surface Science*, vol. 453, pp. 358–364, 2018.
[29] Y. Rafighirani, J. Javidan, and H. Heidarzadeh, "Development of a Multi-Band High-Sensitivity Polarization-Independent Absorber: A Biosensor for Simultaneous Detection of Multiple Cancer Biomarkers," *Plasmonics*, pp. 1–9, 2024.
[30] L. Qi, C. Liu, and S. M. A. Shah, "A broad dual-band switchable graphene-based terahertz metamaterial absorber," *Carbon*, vol. 153, pp. 179–188, 2019.
[31] M. Selvaraj and B. S. Sreeja, "Ultra-sensitive graphene micro-ribbon integrated THz biosensor for breast cancer cell detection," *Methods*, 2025, Accessed: Sept. 18, 2025. [Online]. Available: https://www.sciencedirect.com/science/article/pii/S1046202325001112

[32] M. Ghodrati, A. Mir, and A. Farmani, “Numerical analysis of a surface plasmon resonance based biosensor using molybdenum disulfide, molybdenum trioxide, and MXene for the diagnosis of diabetes,” *Diamond and Related Materials*, vol. 132, p. 109633, 2023.
[33] E. Manikandan, K. A. Karthigeyan, A. Arivarasi, and E. Papanasam, “High-Q and FOM dual-band polarization dependent ultra-narrowband terahertz metamaterial sensor,” *IEEE Photonics Journal*, vol. 15, no. 1, pp. 1–6, 2023.
[34] B. Amini and Z. Atlasbaf, “Design and analysis of high-sensitivity tunable graphene sensors for cancer detection,” *Opt Quant Electron*, vol. 55, no. 5, p. 446, May 2023, doi: 10.1007/s11082-023-04679-y.
[35] D. Liang and T. Chen, “Optical modulated graphene metamaterial based on plasmon-induced transparency in the terahertz band: application for sensing,” *Diamond and Related Materials*, vol. 131, p. 109613, 2023.
[36] H. Bahador, “Five-segment THz refractive index metamaterial biosensor with perfect absorption for carcinoembryonic antigen measurement,” *IEEE Sensors Journal*, 2024, Accessed: Jan. 02, 2025. [Online]. Available: https://ieeexplore.ieee.org/abstract/document/10597354/
[37] B. Khodadadi, P. Rezaei, and S. Hadipour, “Dual-band polarization-independent maze-shaped absorber based on graphene for terahertz biomedical sensing,” *Optics Express*, vol. 33, no. 3, pp. 3869–3880, 2025.
[38] J. Wekalao, N. Mandela, C. Lefu, O. Apochi, C. Wamalwa, and W. Langat, “Terahertz Plasmonic Biosensor Leveraging Ag-Au-Graphene Heterostructures for Quantitative Hemoglobin Analysis with Machine Learning Algorithms for Performance Optimization,” *Plasmonics*, Sept. 2024, doi: 10.1007/s11468-024-02520-0.
[39] B. Khodadadi, M. Babaeinik, V. Ghods, and P. Rezaei, “Sensitivity increment of metamaterial-based refractive index sensor with silicon layers,” *Silicon*, vol. 15, no. 15, pp. 6745–6759, 2023.
[40] M. Abdollahvand, A. H. Azadi, A. Ebrahimifard, and H. Heidarzadeh, “A tunable graphene terahertz sensor with high sensitivity and figure of merit for refractive index biosensing,” *Sci Rep*, Dec. 2025, doi: 10.1038/s41598-025-30606-0.
[41] C. Tan *et al.*, “Cancer Diagnosis Using Terahertz-Graphene-Metasurface-Based Biosensor with Dual-Resonance Response,” *Nanomaterials*, vol. 12, no. 21, p. 3889, Nov. 2022, doi: 10.3390/nano12213889.